START-TO-END SIMULATION OF A NEXT GENERATION LIGHT SOURCE USING THE REAL NUMBER OF ELECTRONS*

J. Qiang† J. Corlett, P. Emma, C.E. Mitchell, C.F. Papadopoulos, G. Penn, M. Reinsch,
R.D. Ryne, M. Venturini, LBNL, USA
S. Reiche, PSI, Switzerland

Abstract

Start-to-end simulation plays an important role in the design and optimization of next generation light sources. In this paper, we will present start-to-end (from the photocathode to the end of the undulator) simulations of a high repetition rate FEL-based Next Generation Light Source driven by a CW superconducting linac with the real number of electrons ($\sim$2 billion electrons/bunch) using the multiphysics parallel beam dynamics code IMPACT. We will discuss the challenges, numerical methods and physical models used in the simulation. We will also present simulation results of a beam transporting through the photoinjector, the beam delivery system, and the final X-ray FEL radiation.

INTRODUCTION

Next generation x-ray light sources provide an important tool for scientific discovery in biology, chemistry, physics, and material science. A high repetition rate, soft x-ray free electron laser (FEL), Next Generation Light Source is being studied at LBNL [1]. High resolution start-to-end macroparticle simulation is an important tool for evaluating and optimizing the design of the light source. For example, a microbunching instability starting from the electron shot noise or initial laser temporal fluctuations can significantly degrade the electron beam quality at the end of the accelerator beam delivery system and lower the resulting performance of the FEL x-ray radiation. Accurate modeling of the microbunching instability with a large number of macroparticles will help to determine the final electron beam properties for generating x-ray radiation. For a given number of macroparticles, N_{mp}, the shot noise in the simulation can be artificially magnified by a factor of $\sqrt{N/N_{mp}}$, where N is the real number of electrons. In previous studies, a low pass filter was proposed to suppress the numerical noise associated with the use of a small number of macroparticles in comparison with the real number of electrons [2]. Applying such a low pass filter does not completely suppress the artificial numerical noise in our simulations. Figure 1 shows the final uncorrelated energy spread at the exit of a beam delivery system using direct sampling of 1 billion macroparticles, 100 million macroparticle sampling with a low pass filter (c1=0.2, c2=0.25) from [2], with a low pass filter (c1=0.03, c2=0.167) and with a low pass filter (c1=0.125, c2 = 0.167). It is seen that even with the
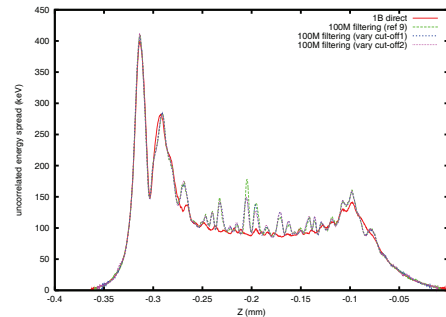
Figure 1: Final uncorrelated energy spread using 1 billion macroparticle direct sampling (red), using 100 million macroparticle sampling with the low pass filter from [2] (c1=0.2, c2=0.25) (green), with a low pass filter and c1=0.03, c2=0.167 (blue), and with a low pass filter and c1=0.125, c2 = 0.167 (pink).
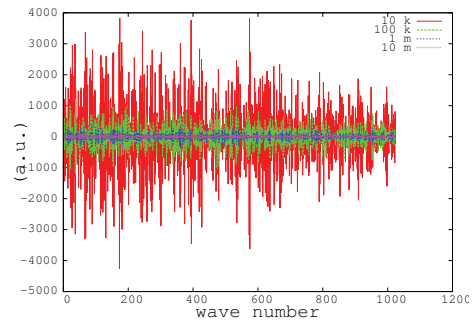
Figure 2: Fourier Coefficient Differences from the FFT of an Analytical Gaussian Function and a Sampled Gaussian Function with 10k, 100k, 1M and 10M Macroparticles.

use of the low pass filter and with different choices of filter parameters, the 100 million macroparticle simulations still predict larger energy modulation than the one-billion macroparticle simulation. In order to understand these effects, we use an FFT to calculate the difference between the Fourier coefficients of an analytical Gaussian function and a randomly sampled Gaussian function using 10 thousand, 100 thousand, one million, and 10 million macroparticles. The results as a function of the mode number (proportional to the wave number of the input) are shown in Fig. 2. It is seen that the sampled shot noise amplitude goes down with the use of a larger number of macroparticles. Sampling using a small number of macroparticles over-estimates the level of shot noise through the whole frequency domain, not just in the high frequency region. A low pass filter helps to suppress the high frequency numerical noise as-
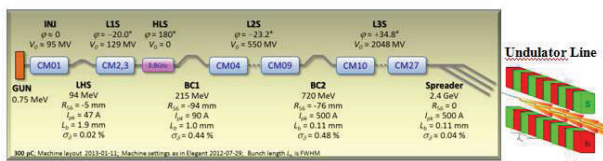
Figure 3: A schematic diagram of the layout of the next generation high repetition rate FEL.

sociated with sampling using a small macroparticle number, but the low frequency numerical noise still exists and increases the final modulation level after being magnified by the microbunching instability through the linac. In our previous study, high resolution beam dynamics simulations were carried out in the study of an old design of the FEL linac and reported in reference [3]. In this paper, we will report on the start-to-end simulation of a new design of the Next Generation Light Source, starting from the photocathode and ending with the final FEL x-ray radiation.

THE LIGHT SOURCE MACHINE LAYOUT

A schematic diagram of the Next Generation Light Source layout is shown in Fig. 3. It consists of a high brightness high repetition rate injector, a high stability CW superconducting linac, a beam spreader, and an array of FEL undulator lines. The injector includes a low RF frequency (187 MHz) high repetition rate (1 MHz or higher) normal conducting gun to generate an electron beam with 750 keV energy, a 1.3 GHz buncher cavity to provide initial velocity bunching, and seven 1.3 GHz Tesla superconducting cavities to accelerate the electron beam energy to about 94 MeV. It is then followed by a laser heater to generate the uncorrelated energy spread in the beam needed to control the effects of the microbunching instability. After the laser heater, two 1.3 GHz Tesla superconducting cavity cryomodules are used to accelerate the electron beam energy to about 215 MeV before entering the first bunch compressor. The first bunch compressor has a momentum compaction factor of $R_{56} = -94.0$ mm, and provides a factor of two compression of the electron beam current. After the first bunch compressor, the electron beam is further accelerated to 720 MeV in six cryomodules before entering the second bunch compressor. This bunch compressor has a momentum compaction factor of $R_{56} = -76.0$ mm and provides another factor of five compression of the electron beam current so that the final beam peak current is between 500 A and 600 A with a total of 300 pC charge. After the second bunch compressor, the electron beam is further accelerated in 18 superconducting cryomodules to a final energy of 2.4 GeV before entering the spreader section, where the 1 MHz electron beam is distributed into different FEL undulator beam lines to generate coherent x-ray radiation. A detailed description of the injector, linac, spreader, FEL undulator, and design concepts of the light source can be found in references [4, 5, 6, 7, 1].
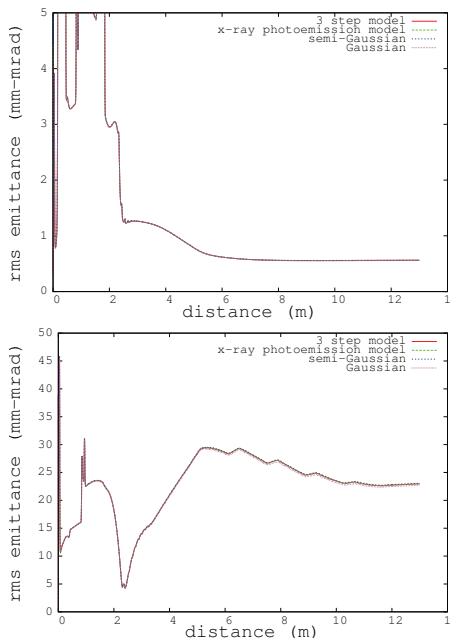
Figure 4: Evolution of horizontal rms emittance (top) and longitudinal rms emittance (bottom) inside the injector from a three-step model (red), a x-ray photoemission model (green), a semi-Gaussian model (blue), and a Gaussian model (pink).
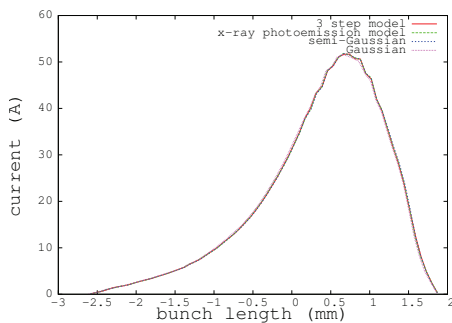
Figure 5: Current profile at the exit of the injector from a three-step model (red), a x-ray photoemission model (green), a semi-Gaussian model (blue), and a Gaussian model (pink).

EFFECTS OF INITIAL DISTRIBUTION

In the start-to-end simulation, the first step is to generate an initial ensemble of macroparticles in six-dimensional phase space. The spatial coordinates of these macroparticles can be sampled following the transverse spatial profile and the longitudinal temporal profile of the input laser pulse. The momentum coordinates of these particles can be generated following some commonly used distributions such as a Gaussian distribution, a semi-Gaussian distribution [8], a x-ray photoemission model [9], or a three-step model [10]. Here, the semi-Gaussian distribution is given
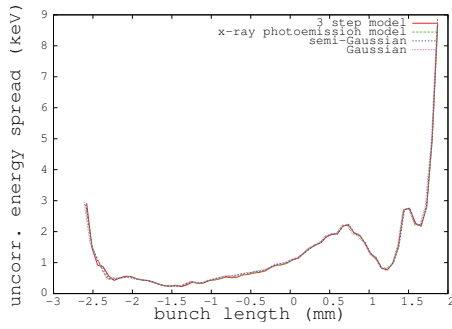
Figure 6: Uncorrelated energy spread along the beam at the exit of the injector from a three-step model (red), a x-ray photoemission model (green), a semi-Gaussian model (blue), and a Gaussian model (pink).

by:

$$f(v_x, v_y, v_z) \quad \propto \quad e^{\left(-\frac{v_x^2}{2\sigma_{v_x}^2} - \frac{v_y^2}{2\sigma_{v_y}^2}\right)} v_z e^{-\frac{v_z^2}{2\sigma_{v_z}^2}}; \ v_z > 0 \quad (1)$$

The x-ray photoemission model is given as:

$$f(E) \quad \propto \quad \frac{E}{(E + E_{wk})^4} \quad (2)$$

$$f(\theta, \phi) \quad \propto \quad \sin(2\theta) \quad (3)$$

where θ is the angle with respect to the normal direction of the cathode surface, and ϕ is the azimuthal angle between 0 and 2π.

In the three-step model, electrons are first excited inside the cathode material by absorption of photons with energy $h\nu$. Then, those electrons migrate to the surface and may experience e-e scattering or e-phonon scattering. In the third step, the electrons with kinetic energy above the barrier potential will escape into the vacuum. To include this model in our simulations, we first assumed an excited electron energy distribution inside the cathode material given by the following:

$$f(E) \quad = \quad (1 - f_{FD}(E))f_{FD}(E - h\nu) \quad (4)$$

where $h\nu$ is the single photon energy of the laser, f_{FD} is the Fermi-Dirac distribution function representing the initial density of the state:

$$f_{FD}(E) \quad = \quad \frac{1}{1 + e^{(E - E_F)/k_B T}} \quad (5)$$

where $k_B T$ is the electron gas thermal energy, and E_F is the Fermi energy. If an electron succeeds in moving to the inner surface of the cathode, a three-dimensional momentum is generated by assuming an angular distribution

$$f(\theta, \phi) \quad = \quad \sin(\theta) \quad (6)$$

After the angular distribution is sampled, the electron transverse and longitudinal momentum can be calculated. Only

an electron with normal momentum satisfying the following condition will be emitted:

$$p_z^{in} = \sqrt{2mE} \cos(\theta) \quad \geq \quad \sqrt{2m(E_F + \phi_{eff})} \quad (7)$$

where ϕ_{eff} is the effective work function of the photocathode material (including both the material work function and the Schottky work function). The transverse and longitudinal momenta for an electron outside the cathode surface will be:

$$p_x \quad = \quad \sqrt{2mE} \sin(\theta) \cos(\phi) \quad (8)$$

$$p_y \quad = \quad \sqrt{2mE} \sin(\theta) \sin(\phi) \quad (9)$$

$$p_z \quad = \quad \sqrt{2m(E - E_F - \phi_{eff}) - p_x^2 - p_y^2} \quad (10)$$

The above process is repeated many times until a specified amount of electron charge is generated.

As a comparison, we ran simulations with above four momentum distribution models while keeping the initial transverse emittance and longitudinal emittance fixed. The spatial distribution was taken to be a uniform cylinder with a 2 ps rising time on both ends. The physical parameter settings of the injector were obtained from a multi-objective optimization discussed in reference [4]. Figures 4-6 show the evolution of the transverse rms emittance and the longitudinal rms emittance through the injector, the beam current profile, and the uncorrelated energy distribution along the beam at the exit of the injector using the above four momentum distribution models. The differences among the simulation results from these momentum distribution models are very small. This might be due to the fact that all these models use the same spatial distribution. In addition, the differences in the initial momentum distribution were quickly washed out by the strong space-charge forces after emission from the photocathode.

EFFECTS OF TRANSVERSE SPACE-CHARGE AROUND LASER HEATER

A laser heater is used after the injector to increase the electron beam uncorrelated energy spread. The transverse rms size of the beam is designed to match the laser spot size (with the same horizontal and vertical sizes) at the center of the undulator in order to optimize the laser electron beam interaction. A diagnostic section right after the laser heater also requires the same sizes in both horizontal and vertical directions. Figure 7 shows the evolution of rms sizes and emittances without and with transverse space charge effects through the matching section, the laser heater, the diagnostic section, and two accelerating modules. Transverse space charge is seen to cause both a mismatch in the envelopes (particularly evident in the vertical plane, red curve) and an emittance growth of more than 20% in the vertical plane, with a smaller growth in the horizontal plane. Such a transverse space-charge induced mismatch can be rematched by tuning the focusing quadrupoles in
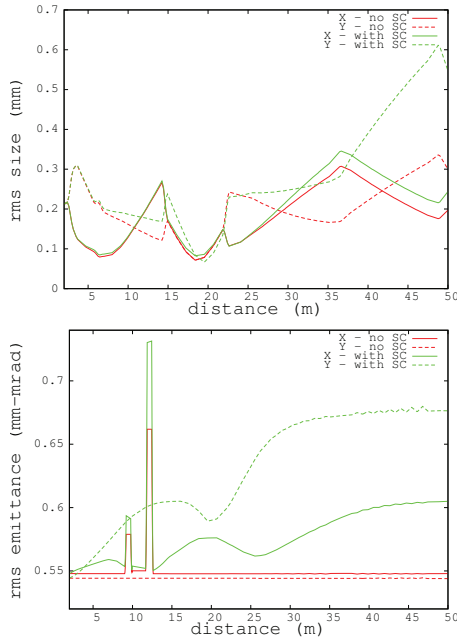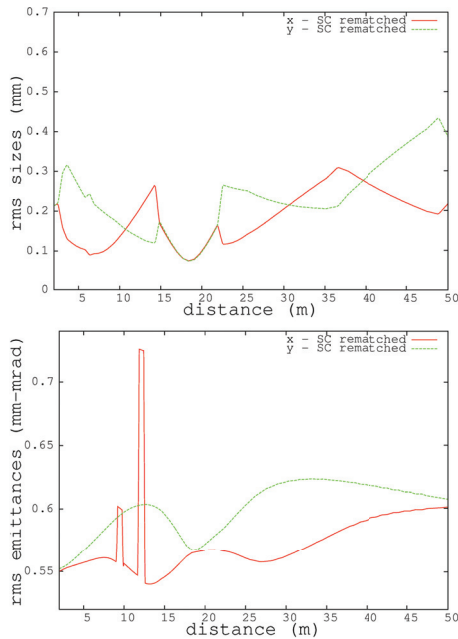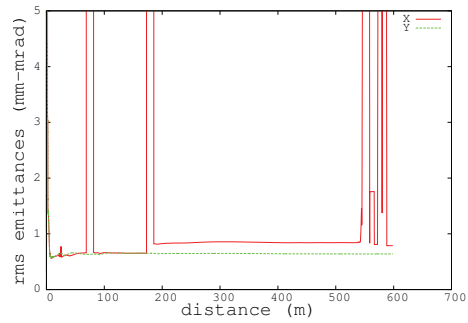
Figure 9: Evolution of transverse rms emittances (red and green) through the whole accelerator beam delivery system.

the matching section after including the transverse space-charge effects. The rms size and emittance evolution of the rematched solution are shown in Fig. 8. It is seen that the envelopes are rematched with correct sizes at the location of the laser heater and inside the diagnostic section. The rms emittance growth is also significantly reduced after rematching the transverse space-charge effects.

START-TO-END SIMULATION OF FEL RADIATION

We carried out a full start-to-end simulation of the FEL x-ray radiation using the real number of electrons (about two billion) in the 300 pC beam. The time-dependent IMPACT-T code [11], the position-dependent IMPACT-Z code [12], and the FEL x-ray radiation GENESIS code [13] are integrated into a single code to facilitate seamless start-to-end simulation in a single run. Here, the IMPACT-T code is used to simulate the photo-electron production and acceleration inside the injector. The IMPACT-Z code is used to simulate the electron beam acceleration, compression and transport through the linac and the spreader. The GENESIS code is used to self-consistently simulate FEL x-ray radiation inside an undulator. The self-consistent 3D space-charge effects, the accelerating cavity structure wakefields, and the CSR wakefields are included in the IMPACT code simulation. The macroparticle electrons pass from the one code to the other code directly through the internal memory of the supercomputer. The whole simulation takes about 10 hours using 2048 cores of a Cray-XE6 supercomputer at the National Energy Research Scientific Computing Center (NERSC). Figure 9 shows the rms emittance evolution through the accelerator beam delivery system. It is seen that the final normalized rms emittances are below 1 mm-mrad. There is a small emittance growth after the second bunch compressor due to CSR effects. A part of the longitudinal phase space distribution of the beam at the end of the beam delivery system is shown in Fig. 10. The uncorrelated energy spread in the relatively flat region is about 150 keV with a peak current between 500 A and 600 A. The multiple billion macroparticles from the exit of the beam delivery system are directly transported into the

Figure 7: Evolution of transverse rms sizes (top) and transverse rms emittances (bottom) without (red) and with (green) space-charge effects in the simulation.

Figure 8: Evolution of transverse rms sizes (top) and transverse rms emittances (bottom) with rematched space-charge effects in the simulation.
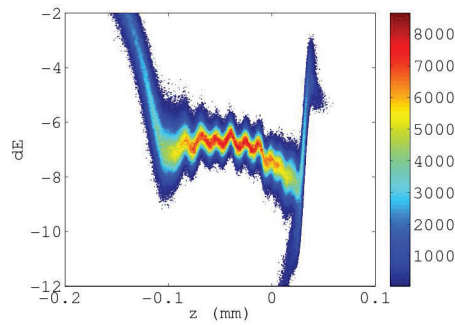
Figure 10: Longitudinal phase distribution at the end of the accelerator beam delivery system.
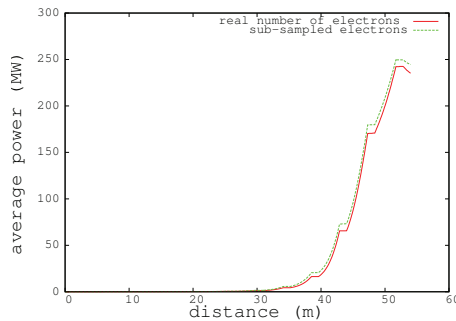
Figure 11: Evolution of the averaged SASE FEL radiation power at the fundamental 1 nm wavelength with the real number of electrons (red) and a subsampled number of electrons (green).

undulator section in the simulation of SASE FEL x-ray radiation. A detailed description of the SASE/self-seeding undulator beam line can be found in reference [7]. Figure 11 shows the average x-ray radiation power evolution along the undulator beam line for the fundamental 1 nm radiation using the real number of electrons (about 2 billion) and a sub-sampled number of electrons (about 450k). The sub-sampled electrons were used in a separate GENESIS simulation with distribution repopulation to approximate the shot-noise in the real electron beam. It is seen from Fig. 11 that the simulations agree well in their predictions of the average power for the fundamental 1 nm x-ray radiation. Figure 12 shows the average power of the 3rd harmonic 0.333 nm radiation as a function of distance in the undulator beam line from both simulations. The simulation using the sub-sampled electrons significantly over predicts the radiation power in comparison with the simulation using the real number of electrons. This could be due to the lack of particle resolution in the transverse phase space that results in the growth of higher order modes besides the Gaussian mode.
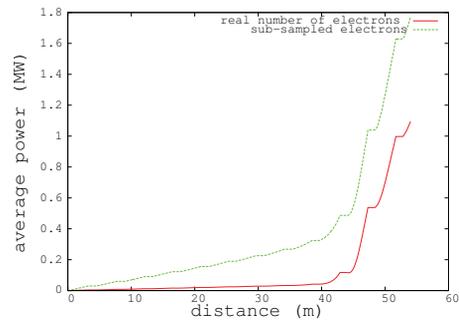
Figure 12: Evolution of the averaged SASE FEL radiation power at 0.3333 nm wavelength with the real number of electrons (red) and a subsampled number of electrons (green).

REFERENCES

[1] J. Corlett, et al., "Design Concepts for a Next Generation Light Source at LBNL," in these Proceedings.

[2] M. Borland, Phys. Rev. ST Accel. Beams 11, 030701 (2008).

[3] J. Qiang et al., Phys. Rev. ST Accel. Beams 12, 100702 (2009).

[4] C. F. Papadopoulos, et al., "Injector Beam Dynamics for a High-repetition Rate 4th-generation Light Source," in Proceedings of IPAC 2012, p. 3000.

[5] M. Venturini, et al., "Beam Dynamics Studies of a High-repetition Rate Linac Driver for a 4th-generation Light Source," in Proceedings of IPAC 2012, p. 1771.

[6] M. Placidi, et al., "Design Concepts for an RF Deflecting Cavity-Based Beam Spreader for a Next Generation FEL," in Proceedings of IPAC 2013, p. 2274.

[7] G. Penn, et al., "Soft X-ray SASE and Self-seeding Studies for a Next-generation Light Source," in Proceedings of FEL 2012, p. 277.

[8] G. A. Bird, *Molecular Gas Dynamics*, Clearndon Press, Oxford, 1976.

[9] B. L. Henke, J. A. Smith, D. T. Attwood, J. Appl. Phys. 48, 1852 (1977).

[10] D. H. Dowell and J. F. Schmerge, Phys. Rev. ST Accel. Beams 12, 074201 (2009).

[11] J. Qiang, S. M. Lidia, R. D. Ryne, C. Limborg-Deprey, Phys. Rev. ST Accel. Beams, Vol 9, 044204 (2006).

[12] J. Qiang et al., J. Comp. Phys. vol. 163, 434, (2000);

[13] S. Reiche, Nucl. Instrum. Methods Phys. Res. A 429, 243 (1999).